In situ x-ray reflectivity studies of dynamics and morphology during heteroepitaxial complex oxide thin film growth

2008 J. Phys.: Condens. Matter 20 264008

(http://iopscience.iop.org/0953-8984/20/26/264008)

J. Phys.: Condens. Matter **20** (2008) 264008 (8pp) doi:10.1088/0953-8984/20/26/264008

In situ x-ray reflectivity studies of dynamics and morphology during heteroepitaxial complex oxide thin film growth

Darren Dale[1,2,5], **Y Suzuki**[3] **and J D Brock**[2,4]

[1] Department of Materials Science and Engineering, Cornell University, Ithaca, NY 14853, USA
[2] Cornell Center for Materials Research, Cornell University, Ithaca, NY 14853, USA
[3] Department of Materials Science and Engineering, UC Berkeley, Berkeley, CA 94720, USA
[4] School of Applied and Engineering Physics, Cornell University, Ithaca, NY 14853, USA

E-mail: dd55@cornell.edu

Received 1 November 2007
Published 9 June 2008
Online at stacks.iop.org/JPhysCM/20/264008

Abstract

We present a method, based on refraction effects in continuous, stratified media, for quantitative analysis of specular x-ray reflectivity from interfaces with atomic-scale roughness. Roughness at interfaces has previously been incorporated into this framework via Fourier transform of a continuous height distribution, but this approach breaks down when roughness approaches the atomic scale and manifests discrete character. By modeling the overall roughness at interfaces as a convolution of discrete and continuous height distributions, we have extended the applicability of this reflectivity model to atomic-scale roughness. The parameterization of thickness and roughness enables quantitative analysis of time-resolved *in situ* reflectivity studies of thin film growth, modeling step-flow, layer-by-layer and three-dimensional growth within a single framework. We present the application of this model to the analysis of anti-Bragg growth oscillations measured *in situ* during heteroepitaxial growth of $La_{0.7}Sr_{0.3}MnO_3$ on $\langle 001 \rangle$ $SrTiO_3$ at different temperatures and pressures, and discuss the evolution of surface morphology.

1. Introduction

Recent advances in growth of epitaxial, complex oxide films and advanced *in situ* growth monitoring techniques have enabled materials engineering with atomic precision via the carefully controlled deposition of sequences of single atomic layers [1–4]. Epitaxial oxide heterostructures are especially attractive, due to the broad range of materials properties that are manifest with changes in stoichiometry, even within a single structure family. Many interesting phenomena have recently been reported, for example, metallic behavior at the interface between two band insulators in $SrTiO_3/LaAlO_3$ heterostructures [5], the origins of which are currently being deliberated [5–8].

Experimentalists are just beginning to explore the possibilities afforded by this degree of control over heteroepitaxial growth. As the community continues to explore phenomena at nearly atomically smooth heteroepitaxial interfaces, it will be increasingly important to understand the influence of disorder and roughness at those interfaces on the materials behavior. X-ray scattering is a valuable technique for studies of surfaces and buried interfaces, including *in situ* studies of the growth and evolution of oxide surfaces and interfaces [9–14]. X-rays have a relatively large penetration depth, which gives rise to interference between radiation scattered from the film surface and the film/substrate interface, known as Kiessig interference [15]. This interference can potentially provide information concerning the density, composition, strain and atomic-scale roughness of the overlayer and therefore enables investigations of, for example, the early stages of nucleation and

[5] Present address: Cornell High Energy Synchrotron Source, Cornell University, Ithaca, NY 14853, USA.

growth. However, we require a single theoretical framework capable of modeling the influence of density, composition, strain and atomic-scale roughness on x-ray reflectivity. For heteroepitaxial growth studies in particular, this framework must also be capable of modeling step-flow, layer-by-layer, and three-dimensional growth.

A problem we have encountered with kinematic scattering models that assign a coverage parameter to each overlayer [16] is that the roughness is coupled to the coverage of each overlayer. Such a model can successfully describe scattering during layer-by-layer or three-dimensional growth, but modeling step-flow growth, where the roughness is not coupled to the coverage of overlayers, is more complicated [17]. Another alternative is to use a dynamical model of reflectivity from continuous, stratified media, but such a model must be able to handle roughness in epitaxial heterostructures at the atomic scale. Previous studies have demonstrated that some types of atomic-scale roughness can manifest with more than one component [14]: a discrete component due to the atomic lattice, and a continuous component due to miscut, surface relaxation, etc. In this report, we quantitatively interpret x-ray reflectivity data using the Abeles–Parratt theoretical framework [18, 19], which we have extended to include discrete roughness on the order of the out-of-plane lattice parameter. By deconvolving the total roughness into discrete roughness (with short in-plane length scales) and continuous roughness (with longer in-plane length scales) components, and decoupling the roughness from the film thickness, we have developed a flexible phenomenological model for analyzing heterostructures with complicated roughness profiles. With this model, it is possible to study pulsed and continuous growth techniques, and a wide variety of growth modes. In this report, we present an analysis of time-resolved studies of epitaxial manganite thin film growth on $\langle 001 \rangle$ $SrTiO_3$.

2. Theory

In the Abeles–Parratt framework, each medium in a heterostructure is considered to be a homogeneous dielectric, with the film thickness treated continuously instead of fractional coverages of discretized thickness [18–20]. The reflected and transmitted amplitudes in each medium, arising from Fresnel reflection due to the changing refractive index at the interface, are found by solving Maxwell's equations. The transmitted and reflected amplitudes t_j and r_j in medium j are related to those in medium $j+1$ by a transfer matrix $\boldsymbol{M}_{j,j+1}$

$$\begin{bmatrix} t_j \\ r_j \end{bmatrix} = \boldsymbol{M}_{j,j+1} \begin{bmatrix} t_{j+1} \\ r_{j+1} \end{bmatrix} = \begin{bmatrix} M_{1,1} & M_{1,2} \\ M_{2,1} & M_{2,2} \end{bmatrix} \begin{bmatrix} t_{j+1} \\ r_{j+1} \end{bmatrix}. \quad (1)$$

The elements of each transfer matrix are a function of the z-component of the wavevector q in each medium surrounding the interface:

$$\begin{aligned} M_{1,1} &= \frac{1}{2}\left(1 + \frac{q_{z,j+1}}{q_{z,j}}\right) \mathrm{e}^{-\mathrm{i}u_{1,1}z_{j,j+1}}, \\ u_{1,1} &= -q_{z,j+1} + q_{z,j} \\ M_{1,2} &= \frac{1}{2}\left(1 - \frac{q_{z,j+1}}{q_{z,j}}\right) \mathrm{e}^{-\mathrm{i}u_{1,2}z_{j,j+1}}, \end{aligned}$$

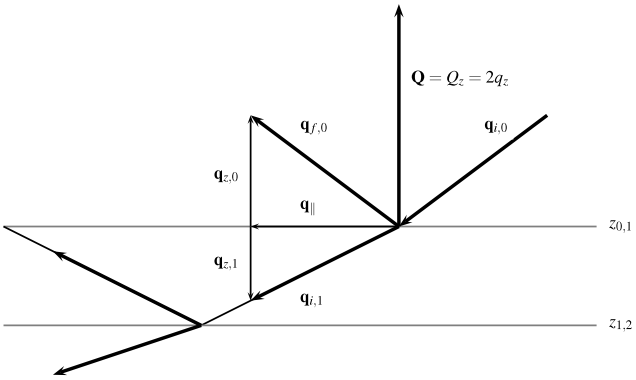

Figure 1. Wavevector diagram for radiation traversing a portion of a heterostructure.

$$\begin{aligned} u_{1,2} &= q_{z,j+1} + q_{z,j} \\ M_{2,1} &= \frac{1}{2}\left(1 - \frac{q_{z,j+1}}{q_{z,j}}\right) \mathrm{e}^{-\mathrm{i}u_{2,1}z_{j,j+1}}, \\ u_{2,1} &= -q_{z,j+1} - q_{z,j} \\ M_{2,2} &= \frac{1}{2}\left(1 + \frac{q_{z,j+1}}{q_{z,j}}\right) \mathrm{e}^{-\mathrm{i}u_{2,2}z_{j,j+1}}, \\ u_{2,2} &= q_{z,j+1} - q_{z,j}. \end{aligned} \quad (2)$$

Each q_z illustrated in figure 1 is a function of the index of refraction in the material, which can be calculated from the density, composition, and the energy-dependent anomalous scattering factors for the elements [21].

Once the transfer matrix $\boldsymbol{M}_{j,j+1}$ is known for each interface, matrix multiplication can be used to recurse through all of the N interfaces and thus determine the characteristic matrix $\mathcal{M}$ for the entire sample [20]

$$\begin{bmatrix} t_0 \\ r_0 \end{bmatrix} = \boldsymbol{M}_{0,1}\boldsymbol{M}_{1,2}\cdots\boldsymbol{M}_{N-1,N} \begin{bmatrix} t_N \\ r_N \end{bmatrix} = \mathcal{M} \begin{bmatrix} t_N \\ r_N \end{bmatrix}. \quad (3)$$

Assuming the reflected amplitude r_N in the thick substrate layer is zero, and setting the incident amplitude $t_0 = 1$, the reflected intensity of the sample, in the absence of roughness, is

$$I = \left|\frac{\mathcal{M}_{2,1}}{\mathcal{M}_{1,1}}\right|^2. \quad (4)$$

For a rough interface, the transmitted and reflected amplitudes $\tilde{t}_j$ and $\tilde{r}_j$ can be calculated with a modified transfer matrix $\tilde{\boldsymbol{M}}_{j,j+1}$ [22]

$$\begin{aligned} \tilde{M}_{1,1} &= M_{1,1}\int_{-\infty}^{\infty} P(z)\mathrm{e}^{-\mathrm{i}u_{1,1}z}\,\mathrm{d}z \\ \tilde{M}_{1,2} &= M_{1,2}\int_{-\infty}^{\infty} P(z)\mathrm{e}^{-\mathrm{i}u_{1,2}z}\,\mathrm{d}z \\ \tilde{M}_{2,1} &= M_{2,1}\int_{-\infty}^{\infty} P(z)\mathrm{e}^{-\mathrm{i}u_{2,1}z}\,\mathrm{d}z \\ \tilde{M}_{2,2} &= M_{2,2}\int_{-\infty}^{\infty} P(z)\mathrm{e}^{-\mathrm{i}u_{2,2}z}\,\mathrm{d}z, \end{aligned} \quad (5)$$

where $P(z)$ is the height distribution about the average position of the interface $\langle z \rangle$. For a continuous Gaussian distribution

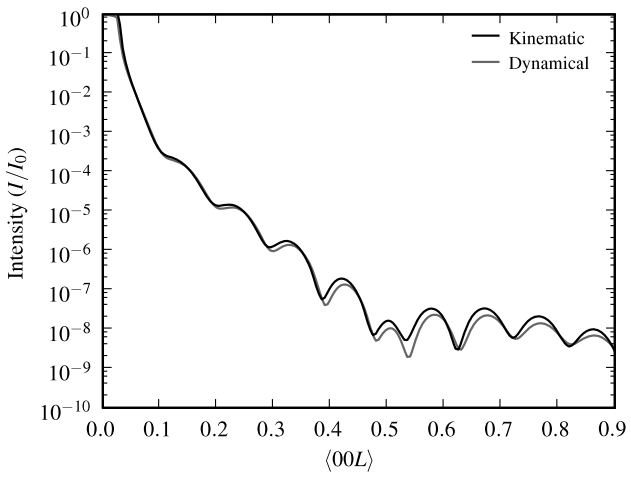

Figure 2. Simulated reflectivity from 10.5 layers of $La_{0.7}Sr_{0.3}MnO_3$ grown in a layer-by-layer mode on $\langle 001 \rangle$ $SrTiO_3$, illustrating the agreement between the dynamical and kinematical models.

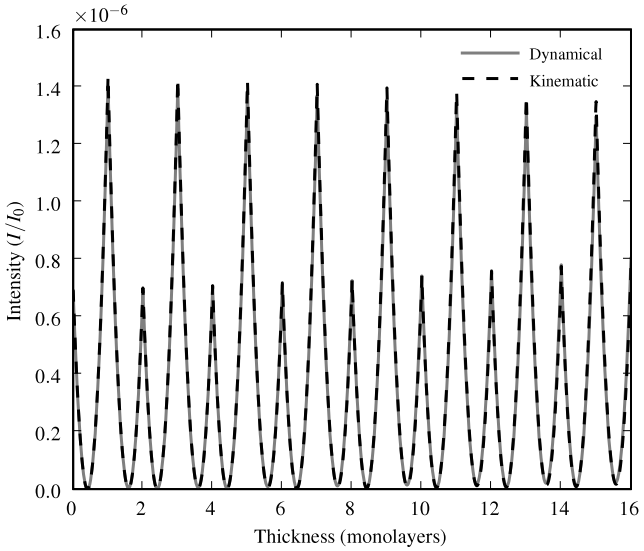

Figure 3. Simulated anti-Bragg growth oscillations during layer-by-layer growth, showing good agreement between the dynamical and kinematical models.

$P_c(z)$, the integrals yield

$$\int_{-\infty}^{\infty} \frac{1}{\sqrt{2\pi}\sigma_c} e^{-(z-\langle z\rangle)^2/2\sigma_c^2} e^{-iuz}\, dz = e^{-u^2\sigma_c^2/2}. \quad (6)$$

A shortcoming of the Fresnel model has been the inability to model roughness on the order of the out-of-plane lattice parameter in epitaxial heterostructures, especially when the roughness and the film thickness are comparable. However, it is possible to describe roughness on these length scales with a convolution of continuous and discrete distributions [14]. Since the roughness is modeled by a Fourier transform of the height distribution, the convolution theorem can be used to model the effects of continuous and discrete contributions independently. The general expression for the Fourier transform of the discrete roughness is

$$\int_{-\infty}^{\infty} P_d(z) e^{-iuz} dz = \int_{-\infty}^{\infty} \sum_{k=0}^{\infty} P_k e^{-iuz} \delta(z - kc_0 + \langle z\rangle) dz, \quad (7)$$

where P_k is the probability that the crystal terminated at level k. The various P_k's are related to the coverage of overlayers θ_k that have been used to model x-ray scattering from surfaces with kinematical theory:

$$\begin{aligned} \theta_n &= P_n \\ \theta_{n-1} &= P_n + P_{n-1} \\ &\vdots \\ \theta_1 &= P_n + P_{n-1} + \cdots + P_2 + P_1. \end{aligned} \quad (8)$$

The binomial distribution is particularly useful for modeling the discrete roughness that arises during pulsed laser deposition of thin films. In the absence of surface diffusion, p is the fraction of the surface covered during a single pulse, n is the number of pulses, and c_0 is the out-of-plane lattice parameter. In this limit, as $n \to \infty$, the distribution becomes Gaussian. The binomial distribution can be used to model perfect layer-by-layer growth by setting $n = 1$ and letting p describe the fractional coverage of the growing monolayer. The Fourier transform of the binomial distribution is

$$\begin{aligned} \int_{-\infty}^{\infty} P_d(z) e^{-iuz}\, dz &= \int_{-\infty}^{\infty} \sum_{k=0}^{n} \binom{n}{k} p^k (1-p)^{n-k} \\ &\quad \times e^{-iuz} \delta(z - kc_0 + npc_0)\, dz \quad (9) \\ &= e^{iunpc_0} \sum_{k=0}^{n} \binom{n}{k} (pe^{-iuc_0})^k (1-p)^{n-k} \\ &= e^{iunpc_0} \left(1 - p + pe^{-iuc_0}\right)^n. \quad (10) \end{aligned}$$

The npc_0 offset inside the delta function in equation (9) is essential to ensure that the distribution is centered about $z_{j,j+1}$, the average position of the interface, thus avoiding a phase offset in the Fourier transform. The last step in deriving equation (10) was made using the binomial theorem.

The transfer matrix for the j, $j+1$ interface, including the effects of both continuous Gaussian and discrete binomial roughness components, is therefore

$$\begin{aligned} \tilde{M}_{1,1} &= M_{1,1}[e^{-u_{1,1}^2\sigma_c^2/2}][e^{iu_{1,1}pc_0}\left(1 - p + pe^{-iu_{1,1}c_0}\right)]^n \\ \tilde{M}_{1,2} &= M_{1,2}[e^{-u_{1,2}^2\sigma_c^2/2}][e^{iu_{1,2}pc_0}\left(1 - p + pe^{-iu_{1,2}c_0}\right)]^n \\ \tilde{M}_{2,1} &= M_{2,1}[e^{-u_{2,1}^2\sigma_c^2/2}][e^{iu_{2,1}pc_0}\left(1 - p + pe^{-iu_{2,1}c_0}\right)]^n \\ \tilde{M}_{2,2} &= M_{2,2}[e^{-u_{2,2}^2\sigma_c^2/2}][e^{iu_{2,2}pc_0}\left(1 - p + pe^{-iu_{2,2}c_0}\right)]^n. \end{aligned} \quad (11)$$

The ability of this model to describe atomic-scale roughness in epitaxial heterostructures is illustrated in figures 2 and 3, where the reflectivity is simulated for $La_{0.7}Sr_{0.3}MnO_3$ grown on $SrTiO_3$ and compared with results from the kinematical model. The model is phenomenological, the roughness can vary independently of the film thickness, and can therefore model specular reflectivity during layer-by-layer, step-flow, and three-dimensional growth, as well as more complicated growth modes that include, for example, simultaneous step-flow and layer-by-layer components.

3. Experimental details

We have studied pulsed laser deposition (PLD) growth of $La_{0.7}Sr_{0.3}MnO_3$ on ⟨001⟩ $SrTiO_3$ using *in situ* x-ray scattering at the Cornell High Energy Synchrotron Source. $La_{0.7}Sr_{0.3}MnO_3$ is interesting due to a high degree of spin polarization at the Fermi level, making it a strong candidate for spin based devices [23–27]. At room temperature, bulk $La_{0.7}Sr_{0.3}MnO_3$ has $R\bar{3}c$ symmetry with $a_0 = 5.5060$ Å, and $c_0 = 13.3564$ Å [28]. In a pseudocubic setting, the lattice parameter is 3.88 Å, resulting in a 0.64% tensile in-plane lattice strain for pseudomorphic films on ⟨001⟩ $SrTiO_3$.

The $SrTiO_3$ substrate is an almost ideal foundation for *in situ* studies of epitaxial film growth. The surface lattice is square, yielding isotropic in-plane strain and diffusion rates. The high quality of commercially available substrates makes them ideal for subsequent electron microscopy studies. ⟨001⟩ $SrTiO_3$ can be treated with a buffered HF etch in order to yield TiO_2 terminated surfaces [29], and it has been reported that SrO terminated surfaces are also be possible [30].

Films were grown from commercially prepared polycrystalline targets using a 248 nm KrF excimer laser with 30 ns pulse duration operating at 1–2 Hz, focused to a 3 mm^2 beam spot, and 3 J cm^{-2} energy density. The target and substrate were in an on-axis geometry with 6 cm separation. Deposition proceeded in either 1 mT or 300 mT O_2, after reaching a base pressure of 10^{-7} Torr. Substrate temperatures varied between samples over the range of 600–1000 °C, as measured with a thermocouple and confirmed with a Modline 3 700 Series pyrometer with a T2 lens. The emissivity of $SrTiO_3$ over the 4.8–5.3 μm range of the pyrometer's operating wavelength was assumed to be 0.8.

During deposition, 10 keV x-rays generated by the Cornell High Energy Synchrotron Source (CHESS) 49 pole wiggler, and monochromated with a set of 1% bandpass multilayers, were directed at the single crystal substrate. The incident x-ray flux at the sample was 10^{11}–10^{12} photons s^{-1}. The growth chamber is an integral part of the diffractometer used to position the sample with respect to the x-ray beam. x-rays were detected using a Bicron NaI(Tl) scintillation point detector located behind a set of guard slits and detector slits. Detector slits were generally 30–50% larger than the cross section of the incident beam. Reflected intensity was measured in the $SrTiO_3\langle 00\frac{1}{2}\rangle$ (anti-Bragg) scattering geometry for maximum sensitivity to discrete roughness with 3.905 Å step height. Microstructure was inspected after deposition using a Digital Instruments Dimension 3100 SPM/AFM, using AFM tips with ≈10 nm radius.

4. Results

The evolution of surface roughness was monitored using *in situ* x-ray scattering in the specular $\langle 00\frac{1}{2}\rangle$ anti-Bragg geometry, and interpreted using the model developed herein. The *in situ* x-ray scattering experiment yields intensity as a function of time. The time axis is transformed into a film thickness, an important parameter for fitting the data. The periodic roughness oscillations arising from imperfect layer-by-layer growth have some phase relationship with the film thickness, which we have modeled with the first Fourier component of a triangle waveform [14]. The total roughness as a function of film thickness is illustrated in figure 4(a). We observe two contributions to the overall roughness. The first is a non-periodic continuous roughness term with power-law relationship to the film thickness $\sigma_c = \sqrt{\sigma_0^2 + (\alpha t^\beta)^2}$, where t is the thickness in Å, $\alpha = 0.38$, $\beta = 0.5$, and σ_0 is the continuous roughness associated with an ideal miscut. The second contribution to the roughness is a periodic discrete roughness term $\sigma_d = c_0\sqrt{p(1-p)}$, modeled using the binomial distribution, arising from the roughness associated with the nucleation, growth and coalescence

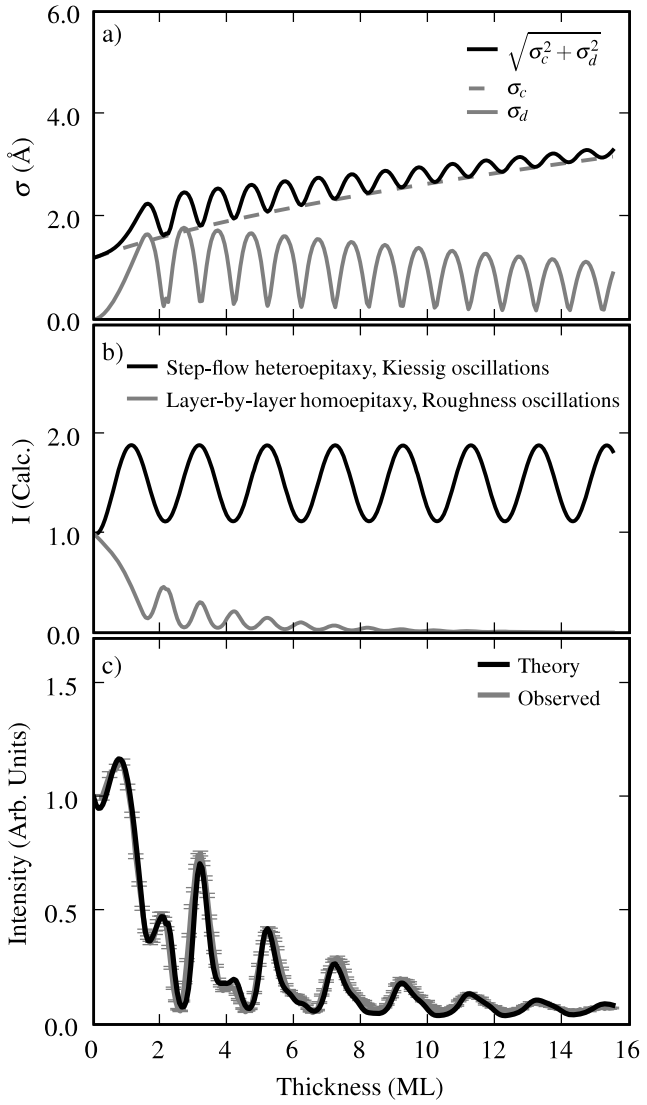

Figure 4. $\langle 00\frac{1}{2}\rangle$ intensity oscillations arising from the growth of $La_{0.7}Sr_{0.3}MnO_3$ on ⟨001⟩ oriented $SrTiO_3$. (a) Simulated RMS roughness. (b) Diffracted intensity from step-flow heteroepitaxial growth, and homoepitaxial growth with evolving roughness as depicted in a. (c) The two effects in plot b are multiplied to give the total heteroepitaxial growth result, which is compared with experiment. The fit indicates that the first half layer deposits smoothly, and three times as fast as subsequent layers.

of small unitcell-tall islands during layer-by-layer growth. The coverage parameter p is modeled using the first term of a Fourier expansion of a triangular wave [14]. The discrete roughness contribution decreases during growth as the continuous roughness increases and the discrepancy between a single Gaussian and the convolution of Gaussian and discrete distributions disappears.

In figure 4(b), simulated heteroepitaxial step-flow growth results in Kiessig oscillations in the anti-Bragg scattering intensity, due to the interference between reflections from the smooth film surface and the interface between film and substrate. Each new monolayer alternately yields a new maximum or a new minimum in the scattered intensity (in the anti-Bragg geometry for the film), thus two monolayers are required to complete each Kiessig oscillation. The only surface roughness associated with step-flow growth is step-edge roughening. Homoepitaxy is also simulated in figure 4(b), which does not exhibit Kiessig interference, but growth oscillations arise from the evolving roughness in figure 4(a), one oscillation per monolayer. It is instructive to imagine that the anti-Bragg intensity during heteroepitaxy would be roughly equivalent to the step-flow result for heteroepitaxy multiplied by the result for evolving roughness during homoepitaxy, yielding a beating in the total signal due to the two oscillation frequencies. This is a useful construction for thinking about the total scattering signal, however, the full analysis of the *in situ* x-ray scattering data for $La_{0.7}Sr_{0.3}MnO_3$ grown on ⟨001⟩ $SrTiO_3$, presented in figure 4(c), requires the model developed herein to account for important but subtle interference effects.

The phase of the roughness oscillation in figure 4(c) is not clearly linked with half-integer or integer film thickness, which we attribute to the presence of surface roughness prior to growth, which forms during heating of $SrTiO_3$ [14]. If the surface were ideally smooth, we would expect an immediate decrease in anti-Bragg intensity during layer-by-layer growth. The absence of such a feature in the reflectivity data during the first half monolayer is a result of this initial roughness. The final thickness of the film is expected to be 15.5 monolayers. The x-ray analysis indicates that the surface roughness was 3.3 Å when growth was terminated.

The post-deposition specular x-ray reflectivity of the sample from figure 4 is shown in figure 5. The out-of-plane lattice parameter for this film was 3.85 Å. The thickness as determined from the reflectivity measurement is 59.7 Å, or 15.5 monolayers, which is in excellent agreement with the model of the *in situ* data. An interesting feature is observed in the specular reflectivity in figure 5 around $L = 0.33$, which could not be fit with continuous Gaussian surface roughness alone. The feature is successfully modeled if discrete roughness is included, in this case discretized at 6.17 Å, or $\approx 1.6c_0$, which we have also observed for $Pr_{0.67}Ca_{0.33}MnO_3$ films. This may indicate the presence of an (La, Sr)O/MnO/MnO or MnO/(La, Sr)O/(La, Sr)O type surface termination. If either MnO_x or $La_{0.7}Sr_{0.3}O_x$ surface termination is strongly preferred, we would expect the roughness to be discretized in units of c_0. If there is not a preferred termination, we would expect the roughness to be discretized in units of $c_0/2$. A third alternative is

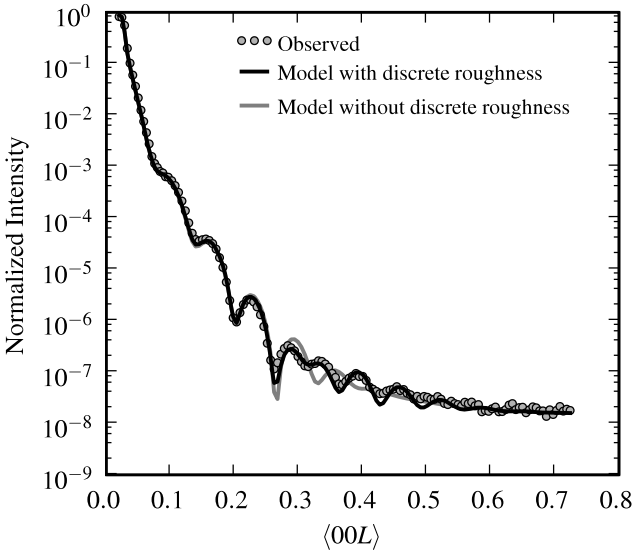

Figure 5. Post-deposition specular x-ray reflectivity of a 15.5 monolayer thick $La_{0.7}Sr_{0.3}MnO_3$ film grown on ⟨001⟩ $SrTiO_3$. The model including discrete roughness is discretized at $1.6 \times c_0$, altering the Kiessig interference around $L = 0.3$.

the formation of the $n = 1$ Ruddlesden–Popper [31] phase $(La_{1-x}Sr_x)_2MnO_4$ at the surface, an analog for which has been observed in $SrTiO_3$ annealed in oxidizing conditions [32]. A Bragg peak near $L = 2/3$ was not observed, indicating that if such a phase exists, it does not extend into the bulk of the film. Some previous reports have indicated that MnO_x is the preferred termination layer for manganite samples annealed at >650 °C in ≈1 atm oxygen for ten or more hours [33–38], while others claim that SrO is the preferred termination layer [39], but repeatedly these studies have concluded that the surface or near surface region is enriched with the divalent dopant, which lends support to the possibility of a Ruddlesden–Popper type phase at the surface.

In situ anti-Bragg intensity data for $La_{0.7}Sr_{0.3}MnO_3$ grown on $SrTiO_3$ at 600, 790 and 950 °C in 1×10^{-3} and 0.3 Torr O_2 are presented in figure 6. A model of the intensity resulting from the continuous roughness contribution is plotted over the experimental results. The growth at 950 °C in 1×10^{-3} Torr O_2 was interrupted after growth of 95, 123, 158, and 188 monolayers to allow the film to anneal. For deposition at 950 °C in both 1×10^{-3} and 0.3 Torr O_2, there is a 2.5-fold decrease and subsequent recovery of scattered intensity during deposition of the first 10 monolayers, where the film initially becomes rough and then appears to enter step-flow growth. In fact, growth at 950 °C appears to be a mix of step-flow and layer-by-layer modes, where an equilibrium concentration of islands is established as evident by the high scattering intensity and decaying contrast of layer-by-layer growth oscillations. When the film is allowed to anneal by interrupting the growth, as seen in figure 7, the anti-Bragg intensity increases due to decreasing discrete roughness, or surface island density. When growth is resumed, the layer-by-layer growth oscillation contrast is again high, but decays as growth continues and the steady-state surface island concentration is reestablished.

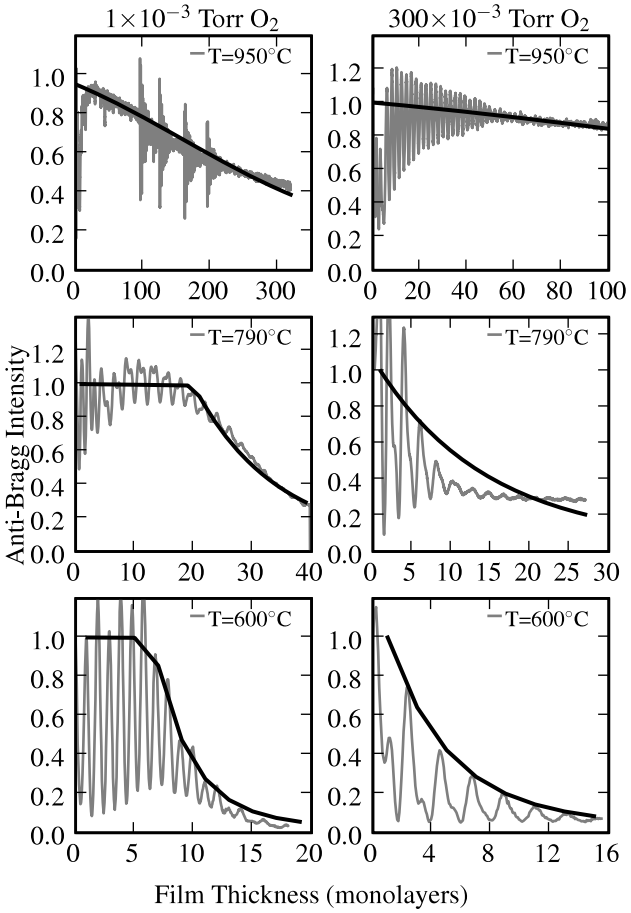

Figure 6. Anti-Bragg intensity versus $La_{0.7}Sr_{0.3}MnO_3$ film thickness, in 1×10^{-3} and 0.3 Torr O_2, for three surface temperatures. The black lines are models of the evolution of continuous surface roughness, with $\beta = 0.5$ power-law thickness dependence.

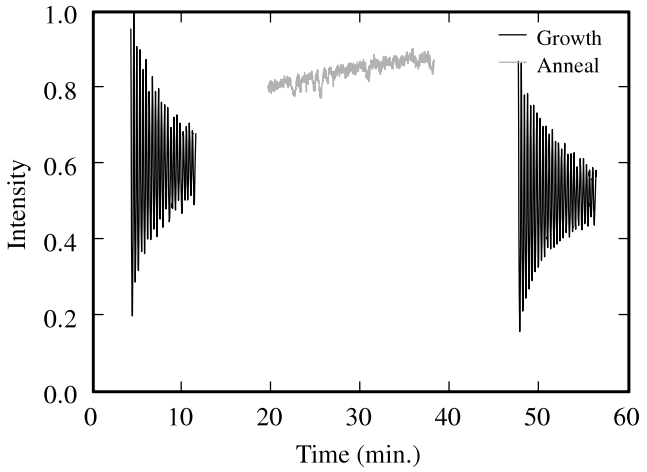

Figure 7. Anti-Bragg intensity versus time. Deposition is shown in black, and annealing in gray. During deposition, layer-by-layer growth oscillation contrast decays as a steady-state step-edge density is established. When growth is interrupted, surface diffusion and possibly evaporation causes the short-range discrete roughness to decrease. When growth is resumed, layer-by-layer growth oscillation contrast is high and decays as the steady-state step-edge density is again established.

Growth at 790 °C in 1×10^{-3} Torr O_2 appears to be a mix of step-flow and layer by layer growth for the first 20 monolayers, after which the film accumulates roughness more quickly. $La_{0.7}Sr_{0.3}MnO_3$ appears to go through a similar roughening transition after growth of 6 monolayers at 600 °C in 1×10^{-3} Torr O_2. In 0.3 Torr, roughness quickly accumulates after the first two layers at 790 °C, and begins to accumulate at the beginning of growth at 600 °C.

Annealing does not appear to affect the continuous roughness component, which is evident in the continuous decline of the steady-state intensity envelope, corresponding to a power-law roughness dependence $\sigma = \alpha t^{\beta}$ where $\beta = 0.5$. Notably, growth in 0.3 Torr O_2 at 950 °C resulted in extended step-flow growth with minimal accumulation of surface roughness. Kiessig oscillations were not present as the growth progressed, but this can be explained by a slightly non-uniform deposition rate across the illuminated surface and the incoherent sum of intensities for regions of different thickness.

The AFM images seen in figure 8 support the interpretation of the *in situ* growth data. Films deposited at high temperature have large crystallites on the surface, but the regions between the crystallites are atomically smooth. Unit cell-high steps are visible for samples grown at 800 °C. In figure 8(a), it is clear that the terraces tend to meander around the particles, resulting in a surface normal distribution which manifests as an increasing continuous roughness contribution (and diffuse scattering) in the *in situ* x-ray data. In figure 8(b), it appears the surface particles are just beginning to form (they are roughly 10% as tall as those in figure 8(a)), and have not yet affected the terraced microstructure. Deposition at lower temperature results in a much quicker loss of the initial terraced surface structure, stronger short-range correlations and weaker long-range correlations, as seen in figures 8(c)–(f).

Deposition at elevated temperatures could yield the atomically sharp surfaces desired for advanced applications, were it not for the massive crystallites forming on the film surface. These crystallites, which were only observed with $La_{0.7}Sr_{0.3}MnO_3$ films grown at 950 °C, appear to form in an equilibrium process due to a supersaturation of some species at the surface. The composition of surface crystallites on a 431 monolayer thick film was investigated with x-ray fluorescence spectroscopy using a JEOL 8900 EPMA Microprobe, as seen in figure 9. The crystallites are typically $\leqslant$150 nm tall and 200–400 nm wide, which is relatively small compared to the $\approx$1 μm lateral resolution of the instrument. Fluorescence spectra from the crystallites will therefore include signal from the film as well, due to the small size of the particles. However, the Sr, La and Ti fluorescence signals are all weaker for the particle than the film, while the Mn signal is stronger for the particles. The Ti fluorescence signal, measured at 10 keV, is $30 \pm 3\%$ weaker in the particle spectrum, due to the increased path-length to the substrate. The $22 \pm 2\%$ decrease in Sr fluorescence from the particle is due in part to the increased path-length to the $SrTiO_3$ substrate through the particle, but may also be due to a depletion of Sr in the crystallites. The La signal from the particle is also decreased by $22 \pm 2\%$, which indicates that the crystallites are La-deficient. The Mn signal is increased by

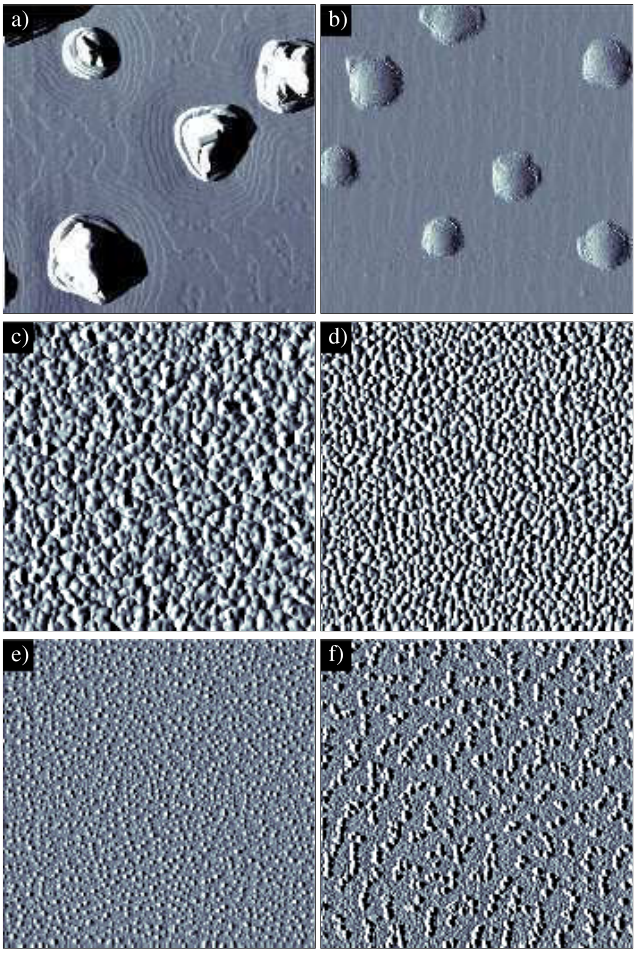

Figure 8. 2 μm $\times$ 2 μm tapping mode AFM images of $La_{0.7}Sr_{0.3}MnO_3$ films, as measured in amplitude mode. (a) $T_s = 800\,^{\circ}C$, $P = 1 \times 10^{-3}$ Torr O_2. (b) $T_s = 800\,^{\circ}C$, $P = 0.3$ Torr O_2. (c) $T_s = 640\,^{\circ}C$, $P = 1 \times 10^{-3}$ Torr O_2. (d) $T_s = 640\,^{\circ}C$, $P = 0.3$ Torr O_2. (e) $T_s = 520\,^{\circ}C$, $P = 1 \times 10^{-3}$ Torr O_2. (f) $T_s = 520\,^{\circ}C$, $P = 0.3$ Torr O_2. The voltage range is identical for every image, the steps in (a) are 4 Å.

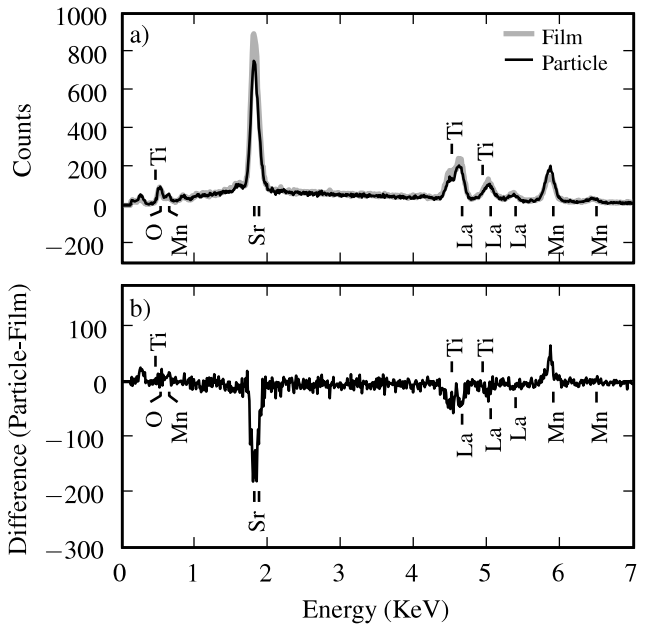

Figure 9. (a) X-ray fluorescence spectra of an $La_{0.7}Sr_{0.3}MnO_3$ film grown at 950 °C, and of an associated surface particle. (b) Difference spectra (particle–film), indicating Mn rich and Sr-deficient particle composition.

$45 \pm 5\%$ in the particle. Thus the crystallites appear to be rich in manganese, lanthanum deficient, and most likely strontium deficient.

5. Conclusions

We have investigated the early stages of nucleation and growth of $La_{0.7}Sr_{0.3}MnO_3$ on $\langle 001 \rangle$ $SrTiO_3$ using a highly surface-sensitive *in situ* x-ray scattering technique. The small scattering cross section of x-rays results in a large penetration depth, yielding information about buried interfaces which can be inaccessible with electron scattering probes. We have developed a method for the quantitative analysis of *in situ* x-ray scattering during growth of multilayers using the Abeles–Parratt framework, which we have extended to account for discrete binomial surface roughness on the order of the out-of-plane lattice parameter. This model allows each interface to be treated statistically, by deconvolving discrete and continuous roughness components. Furthermore, the roughness is decoupled from the film thickness, which provides the flexibility necessary to model many different types of growth. This model was used for analysis of the evolution of x-ray reflectivity during pulsed laser deposition growth.

Experimental results indicate that as growth proceeds, the discrete roughness associated with layer-by-layer growth decreases as the continuous roughness increases. Post-deposition reflectivity scans suggest the presence of roughness discretized at 1.6 unit cells, which, in conjunction with previous reports of Sr, Ca and Pb segregation to the surface of manganite films in oxidizing environments, may indicate the presence of an $n = 1$ Ruddlesden–Popper type phase at the surface.

For growth at 950 °C, we have observed that the short-range surface roughness, and therefore the surface island density, approaches a steady-state value, while the long-range roughness continues to accumulate with power-law behavior, with exponent of 0.5. AFM images confirm that at 950 °C, a terraced microstructure with 4 Å steps is visible in the regions between the surface particles, indicating some component of step-flow in the growth mechanism. The evolution of the long-range surface roughness is strongly influenced by the formation of surface crystallites, which impede the motion of flowing step-edges and result in a surface with an increasingly wide surface normal distribution. The formation of surface crystallites should be investigated further. If not for the presence of these features on the surface, it appears that growth would largely occur via a sustainable step-flow mechanism, and would yield the ideal surfaces and interfaces that are widely sought for future applications.

Acknowledgments

We would like to acknowledge Aaron Fleet for prior work on this project and continued helpful discussions. We would also like to acknowledge John Hunt for his help with the microprobe. This work was funded in part by the Cornell Center for Materials Research (CCMR). Support for the CCMR is provided through the NSF Grant DMR-0520404, part of the NSF MRSEC Program. This work is based upon research conducted at the Cornell High Energy Synchrotron Source (CHESS) which is supported by the National Science Foundation and the National Institutes of Health/National Institute of General Medical Sciences under award DMR 0225180. The plots presented were generated using open source software. DD would like to acknowledge the developers of Python, Matplotlib and Scipy.

References

[1] Iijima K, Terashima T, Bando Y, Kamigaki K and Terauchi H 1992 *J. Appl. Phys.* **72** 2840
[2] Tsurumi T, Suzuki T, Yamane M and Daimon M 1994 *Japan. J. Appl. Phys.* 1 **33** 5192
[3] Tabata H, Tanaka H and Kawai T 1994 *Appl. Phys. Lett.* **65** 1970
[4] Takahashi R, Matsumoto Y, Koinuma H, Lippmaa M and Kawasaki M 2002 *Appl. Surf. Sci.* **197** 532
[5] Ohtomo A and Hwang H 2004 *Nature* **427** 423
[6] Herranz G, Basletic M, Bibes M, Carretero C, Tafra E, Jacquet E, Bouzehouane K, Deranlot C, Hamzic A and Broto J M 2007 *Phys. Rev. Lett.* **98** 216803
[7] Kalabukhov A, Gunnarsson R, Borjesson J, Olsson E, Claeson T and Winkler D 2007 *Phys. Rev.* B **75** 121404
[8] Siemons W, Koster G, Yamamoto H, Harrison W A, Lucovsky G, Geballe T H, Blank D H A and Beasley M R 2007 *Phys. Rev. Lett.* **98** 196802
[9] Eres G, Tischler J Z, Yoon M, Larson B C, Rouleau C M, Lowndes D H and Zschack P 2002 *Appl. Phys. Lett.* **80** 3379
[10] Fleet A, Dale D, Suzuki Y and Brock J 2005 *Phys. Rev. Lett.* **94** 036102
[11] Fleet A, Dale D, Woll A R, Suzuki Y and Brock J D 2006 *Phys. Rev. Lett.* **96** 055508
[12] Willmott P R, Herger R, Schleputz C M, Martoccia D and Patterson B D 2006 *Phys. Rev. Lett.* **96** 176102
[13] Tischler J, Eres G, Larson B, Rouleau C M, Zschack P and Lowndes D H 2006 *Phys. Rev. Lett.* **96** 226104
[14] Dale D, Fleet A, Suzuki Y and Brock J D 2006 *Phys. Rev.* B **74** 085419
[15] Kiessig H 1931 *Ann. Phys. Lpz.* **11** 645
[16] Robinson I K 1986 *Phys. Rev.* B **33** 3830
[17] Myers-Beaghton A and Vvedensky D 1990 *Phys. Rev.* B **42** 9720
[18] Abeles F 1950 *Ann. Phys., Lpz.* **5** 596
[19] Parratt L 1954 *Phys. Rev.* **95** 359
[20] Born M and Wolf E 1999 *Principles of Optics* 7th edn (Cambridge: Cambridge University Press) chapter 1, pp 58–74
[21] Als-Nielsen J and McMorrow D 2001 *Elements of Modern X-ray Physics* (New York: Wiley) chapter 3, pp 61–70
[22] Vidal B and Vincent P 1984 *Appl. Opt.* **23** 1794
[23] Sun J Z, Gallagher W J, Duncombe P R, KrusinElbaum L, Altman R A, Gupta A, Lu Y, Gong G Q and Xiao G 1996 *Appl. Phys. Lett.* **69** 3266
[24] Park J-H, Vescovo E, Kim H-J, Kwon C, Ramesh R and Venkatesan T 1998 *Nature* **392** 79
[25] Park J-H, Vescovo E, Kim H-J, Kwon C, Ramesh R and Venkatesan T 1998 *Phys. Rev. Lett.* **81** 1953
[26] Nadgorny B, Mazin I, Osofsky M, Soulen R, Broussard P, Stroud R, Singh D, Harris V, Arsenov A and Mukovskii Y 2001 *Phys. Rev.* B **63** 184433
[27] Nadgorny B 2007 *J. Phys.: Condens. Matter* **19** 315209
[28] Radaelli P, Iannone G, Marezio M, Hwang H, Cheong S-W, Jorgensen J and Argyriou D 1997 *Phys. Rev.* B **56** 8265
[29] Kawasaki M, Takahashi K, Maeda T, Tsuchiya R, Shinohara M, Ishiyama O, Yonezawa T, Yoshimoto M and Koinuma H 1994 *Science* **266** 1540
[30] Schrott A G, Misewich J A, Copel M, Abraham D W and Zhang Y 2001 *Appl. Phys. Lett.* **79** 1786
[31] Ruddlesden S N and Popper P 1957 *Acta Crystallogr.* **10** 538
[32] Szot K and Speier W 1999 *Phys. Rev.* B **60** 5909
[33] McIlroy D, Waldfried C, Zhang J, Choi J-W, Foong F, Liou S and Dowben P 1996 *Phys. Rev.* B **54** 17438
[34] Yoshimoto M, Maruta A, Ohnishi T, Sasaki K and Koinuma H 1998 *Appl. Phys. Lett.* **73** 187
[35] Izumi M, Konishi Y, Nishihara T, Hayashi S, Shinohara M, Kawasaki M and Tokura Y 1998 *Appl. Phys. Lett.* **73** 2497
[36] Choi J, Zhang J, Liou S-H, Dowben P and Plummer E 1999 *Phys. Rev.* B **59** 13453
[37] Choi J, Dulli H, Liou S-H, Dowben P and Langell M 1999 *Phys. Status Solidi* b **214** 45
[38] Borca C, Ristoiu D, Xu Q, Liou S, Adenwalla S and Dowben P 2000 *J. Appl. Phys.* **87** 6104
[39] Bertacco R, Contour J P, Barthelemy A and Olivier J 2002 *Surf. Sci.* **511** 366